ISBN: 978-3-95450-223-3 ISSN: 2673-7000 doi:10.18429/JACoW-NAPAC2019-TUXBA3

ROBUST THERMOACOUSTIC RANGE VERIFICATION FOR PULSED ION BEAM THERAPY

S. K. Patch†, UW-Milwaukee, Milwaukee, WI USA
B. Mustapha, D. Santiago-Gonzalez, Argonne National Laboratory, Lemont, IL USA

Abstract

Particle therapy is a high-risk option compared to conventional x-ray radiation because dose is concentrated near the Bragg peak. Patient misalignment can cause greater damage to healthy tissue and failure to completely treat the tumour. Therefore, relatively few tumour sites are deemed appropriate for particle therapy.

Thermoacoustic range verification is enabled by intense pulsed beam delivery and might enable treatment of soft tissue tumors, but range estimates are shifted by soundspeed variations within the patient.

Soundspeed errors dilate and acoustic heterogeneities deform ultrasound images. When thermoacoustic receivers are co-located with the ultrasound imaging array, the same transformations shift thermoacoustic range estimates. Therefore, thermoacoustic range verification is robust relative to ultrasound images of underlying anatomy and could be directly used when the treatment target is visible in ultrasound.

INTRODUCTION

Range verification is currently the weak link in ion therapy. Range verification techniques such as prompt gamma, positron emission tomography, and cone beam computerized tomography (CBCT) lack direct correlation to live images of underlying anatomy. CBCT exposes organs at risk (OARs) to ionizing radiation and the primary benefit of ion therapy is to spare OARs.

Thermoacoustics could provide online range verification with direct correlation to underlying morphology as depicted in ultrasound images (Fig. 1), and without exposing OARs to ionizing radiation. However, thermoacoustic range estimates in absolute (room) coordinates are skewed by acoustic heterogeneities, and even by assuming an incorrect soundspeed in a homogeneous target. Incorrect soundspeed settings and acoustic heterogeneities dilate and deform ultrasound images respectively. We demonstrate that thermoacoustic estimates of the Bragg peak location (Fig. 1(b)) are subject to the same transformations as ultrasound images when thermoacoustic receivers are co-located with ultrasound imaging arrays.

Thermoacoustic signals were detected in national laboratories [1, 2] and proposed for range verification during particle therapy [3, 4] decades ago. Synchrocyclotrons deliver stress-confined pulses that may enable thermoacoustic range verification [5], as will linacs designed for therapy [6]. A resurgence in thermoacoustic research, generating too many papers to cite is described in recent reviews [7, 8]. A brief overview of results that correlate range estimates with ultrasound follows.

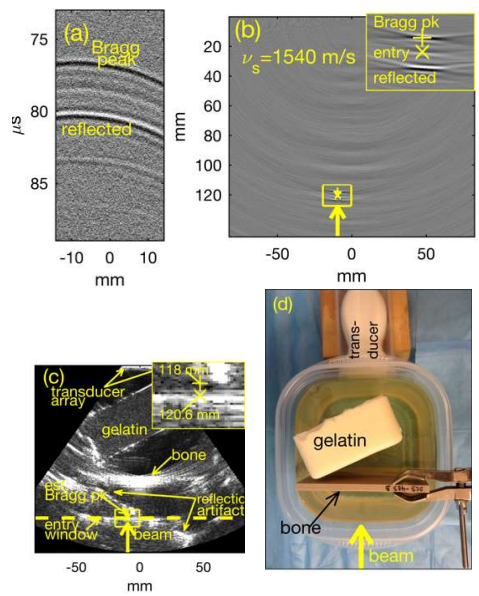

Fig. 1. Thermoacoustic range verification despite acoustic heterogeneity. Thermoacoustic emissions from a single 4He pulse (a) and thermoacoustic image (b) from which Bragg peak location, range, and beam entry point are estimated. (c) Ultrasound image of acoustic scatterers in an oil target with thermoacoustic estimates overlaid. Bragg peak and ion entry locations are overlaid as yellow '+' and 'x'. Estimated beam entry window plotted in dashed yellow. (d) Aerial photo depicting the experimental setup.

A linear array was used to generate ultrasound images that were co-registered to images reconstructed from thermoacoustic emissions measured by a curved array, requiring digital co-registration [9]. To our knowledge, our previous work [10] is the only one that provides inherent co-registration of thermoacoustic range estimates with ultrasound images of underlying anatomy, by using the same ultrasound array to detect thermoacoustic emissions and generate ultrasound images. Thermoacoustic emissions in this report were tailored to the ultrasound array's frequency band, reducing the required dose by three orders of magnitude. 2.3 Gy produced thermoacoustic emissions in Fig. 1(a) from which accurate range estimates were generated. Additionally, in this work we estimate Bragg peak locations from thermoacoustic emissions that traveled through a strongly scattering bone sample (Fig. 1(c)). Finally, we demonstrate robustness and accuracy of thermoacoustic range estimates relative to ultrasound images with fields of view exceeding 60 mm, despite acoustic heterogeneity and incorrect soundspeed settings on the scanner.

Content from this work may be used under the terms of the CC BY 3.0 licence (© 2019). Any distribution of this work must maintain attribution to the author(s), title of the work, publisher, and DOI

ISBN: 978-3-95450-223-3 ISSN: 2673-7000 doi:10.18429/JACoW-NAPAC2019-TUXBA3

MATERIALS AND METHODS

Experiments were performed at the ATLAS facility of Argonne National Laboratory [11]. Data was acquired on a programmable ultrasound system using different sound-speed settings and homogeneous and heterogeneous targets to demonstrate robustness relative to ultrasound images, despite soundspeed errors and acoustic heterogeneity. Monte Carlo simulations were performed to model the energy deposited by stopping ion because induced pressure is proportional to energy density. Details are in [12].

Beam Specifications

A series of 12-MHz superconducting resonators accelerated proton and helium-4 (4He) ions for two different experiments. A 4He beam was accelerated to 60.7 ± 0.4 MeV and a proton beam to 15.99 ± 0.15 MeV in the first and second experiments, respectively.

Both proton and 4He beams exited the beam line through a 25 µm titanium foil and entered liquid targets through 60 µm acrylic packing tape (Staples). 4He ions and protons travelled through 2 cm and 19 cm of air between exit foil and the target, respectively. Horizontal and vertical beam cross sections were asymmetric, as measured using beam profile monitors located 26" upstream of the targets.

A beam sweeper allowed 3 of 120,000 RF cycles to pass to the target at a pulse repetition frequency of 100 Hz. Ion pulse duration was confirmed using a photomultiplier tube with fast plastic scintillator placed below and behind the targets during proton and 4He runs, respectively. The PMT detected O(10) gammas per ion pulse delivered to the target, so pulses were averaged on the scope to generate smooth pulse profiles in Fig. 2(a). (512 and 1024 PMT pulses were averaged for protons and 4He, respectively.) Phase error of the sweeper during the 4He run resulted in severe truncation of the third bunch, which smoothed the spectra of the pulse envelope, but also increased essential bandwidth from 4 MHz=1/250 ns (proton) to 6 MHz = 1/167 ns (4He), as shown in the inset in Fig. 2(b).

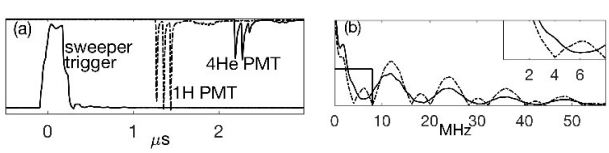

Fig. 2. Trigger and PMT traces from 4He and proton runs in time (a) and frequency (b) domains. PMT traces for protons and helium-4 plotted in dashed and solid, respectively.

Targets / Phantoms

Water and safflower oil were the background fluids during the proton and 4He runs, respectively. Water has the advantages of extremely low acoustic attenuation and well-known physical properties, whereas safflower oil has the advantage of more realistic acoustic attenuation and approximately three-fold higher specific heat capacity, which leads to more efficient thermoacoustic signal generation. Tissue mimicking gelatin and bone samples provide diffuse and strong acoustic scatterers.

- *Water with air-gap phantom.* An aluminum phantom was machined to a thickness of 6.5 mm, and the 60 µm packing tape sealed a 4 cm diameter hole on each end. To vary the beam range within the water-filled tank, the phantom was suspended below a stepper motor (Haydon-Kerk DCM-8028), with translation range of 10 cm. A counterweight was added to ensure that the phantom stayed nearly flush to the entry port during translation. Nevertheless, protons traversed approximately 1 mm of water between entry port and phantom.
- *Oil with TM gelatin and bone.* The 5 mm bone sample (CIRS #DCB-403B) was placed approximately 4 cm distal to the beam entry point so the beam stopped in oil, rather than in the bone sample. Thermoacoustic emissions traveled through the oil, bone sample and a 35 mm thick layer of tissue mimicking gelatin containing diffuse acoustic scatterers before reaching the ultrasound array. As viewed in the ultrasound imaging plane the entry tape and bone sample were positioned parallel to the array, whereas the gelatin was rotated approximately 45-degrees, (see Fig. 1).

Acoustic Hardware

Data was acquired by a 96-channel ultrasound array with 6 dB bandwidth of 1-4 MHz (ATL, P4-1) attached to a programmable ultrasound system (Verasonics V1). The V1 and host computer were positioned several feet below the ion beam. The ultrasound array was placed on the beam trajectory, distal to the Bragg peak. 100' VGA and USB cables connected the host computer to peripherals (monitor, keyboard and mouse) located outside the vault. Data acquisition was triggered by the logic signal shown in Fig. 2(a), which was split, with one line to V1 and other to the oscilloscope located outside.

Data Processing / Consistency Checks

Data processing was modified from our previous work [10] to overlay the Bragg peak location during thermoacoustic data acquisition, rather than offline. During the proton run, the ultrasound image was updated for each new thermoacoustic range estimate. Additional software modifications included 2x upsampling in time prior to one-way beamforming onto an image lattice that was 4x upsampled in the longitudinal direction relative to the ultrasound image and providing estimates of the beam entry depth in addition to the Bragg peak location.

Two consistency checks were applied to our results. First, range estimates were compared to Monte Carlo simulations. Second, the beam entry position was estimated from thermoacoustic images and then compared to ultrasound images that visualize the beam entry window.

Thermoacoustic signals generated in homogeneous targets often have a characteristic "3-stripe" signature (Fig. 1(a)). The first stripe emanates from the Bragg peak and travels directly to the receiver. The second stripe emanates from the beam entry point, has opposite polarity to the first stripe, travels directly to the receiver and is typically weaker. The third stripe emanates from the Bragg peak, reflects off the entry window and travels to the receiver with polarization unchanged. The stripes manifest

Content from this work may be used under the terms of the CC BY 3.0 licence (© 2019). Any distribution of this work must maintain attribution to the author(s), title of the work, publisher, and DOI

ISBN: 978-3-95450-223-3 ISSN: 2673-7000 doi:10.18429/JACoW-NAPAC2019-TUXBA3

Content from this work may be used under the terms of the CC BY 3.0 licence (© 2019). Any distribution of this work must maintain attribution to the author(s), title of the work, publisher, and DOI

themselves in thermoacoustic images as three marks separated in the depth direction by the beam range into the target (Fig. 1(b)). Range estimates were based upon direct and reflected thermoacoustic signals from the Bragg peak.

Range was added to the depth of the Bragg peak location to estimate where the beam entered the target. Although Bragg peak locations cannot be seen in ultrasound images, the entry depth into the target is almost always visible because interfaces between materials of different stopping power typically cause acoustic reflections. Therefore, accuracy of beam entry depth estimates derived from thermoacoustic images were validated relative to the ultrasound images.

RESULTS

He into oil with TM gelatin and 5 mm bone

In this case the imaging field of view was larger and the bone sample was placed 4 cm distal to the Bragg peak, so 4He ions stopped in safflower oil, mimicking a benchtop example published about a single element transducer transmitting a pulse to an ultrasound array [13].

No signal averaging was required because thermoacoustic pulse amplitudes were higher for multiple reasons: each 4He ion deposited fourfold the energy near the Bragg peak of a proton, seven-fold more efficient conversion of thermal to mechanical energy in oil ($\Gamma = 0.7$) compared to water ($\Gamma = 0.1$), and higher beam current during the 4He run, 5.5 M ions/pulse. Additionally, deposited energy maps differed because relative energy spread for 4He was smaller than for the proton beam (0.6% vs 0.9%), but the proton beam was more tightly focused. TRIM simulations showed that the per ion energy density along the central 1 mm was 3.9e-7 kJ/m^3 for the helium beam. Density of cooking oils is approximately 900 kg/m^3, so the 4He beam delivered approximately 2.3 Gy per pulse.

The presence of bone and gelatin repeatably shifted the average estimate of the Bragg peak *z*- and *x*- locations by 3.7 mm and 2.8 mm, commensurate with contraction of the ultrasound image. Range estimates were initially computed assuming soundspeed of 1540 m/s, because that was used to create the ultrasound image in Fig. 1. Recomputing the range with the soundspeed of oil reduces range estimates to within 250 μm of the Monte Carlo simulations.

Protons into water with air-gap phantom

Data acquisition commenced using Verasonics' default soundspeed setting of 1540 m/s. The soundspeed setting was then reduced to 1480 m/s to match that of water. The measured time series remained unchanged, while the thermoacoustic estimates and ultrasound images contracted. Then, an air gap was introduced within approximately 1 mm of the entry tape. Thermoacoustic emissions arrived earlier and were not as well separated because the air gap phantom was not perfectly flush with the entry wall. Protons travelled some distance in water before encountering the air gap, reducing their range after exiting the air gap. Nevertheless, the estimate of the Bragg peak location shifted by 6.6 mm, from 61.5 mm.

DISCUSSION

In this work we demonstrated that thermoacoustic range verification is robust *relative to the ultrasound image of underlying anatomy* and may be feasible in the presence of bone and air gaps.

Thermoacoustics may prove a clinically effective and relatively inexpensive range verification technique for particle therapy. Incorporating ultrasound systems into ion therapy vaults could provide low-cost, small-footprint, and non-ionizing online image-guided therapy. Customized ultrasound systems would be slightly more expensive but could also provide online range verification that is inherently co-registered to the underlying ultrasound image.

Weaknesses of thermoacoustic range verification are that it is only appropriate for targets that can be imaged by ultrasound and that thermoacoustic emissions have low amplitude. In soft tissue, the factors converting dose into pressure range from approximately 2 Pa/cGy in muscle and organs to 8 Pa/cGy in fat and 15 Pa/cGy in bone [14], Only 1 Pa/cGy is generated in water, but thermoacoustic emissions generated by a clinical synchrocyclotron in a water bath have been detected [5].

A weakness of this study is the fact that low beam energies were required to generate thermoacoustic emissions that our current acoustic hardware can detect and overlay onto ultrasound images. Nevertheless, range estimates were obtained by backprojecting (or one-way beamforming) over distances exceeding 60 mm, so 300 μm error represents only 0.5% of the distance between the transducer array and Bragg peak. Furthermore, thermoacoustic estimates of the ion beam's entry point into the target agreed with ultrasound images of the air-target interface, providing confidence in range estimates relative to the underlying ultrasound images.

Bandwidth of thermoacoustic emissions should be matched to acoustic receivers. Range straggle of protons and 4He ions with range exceeding 20 cm bandlimits thermoacoustic emissions below 100 kHz. In practice, emissions are further bandlimited by the ion pulse envelope [15–17] and measurements are bandlimited by the receive hardware. Custom acoustic transducers will be required to detect both low frequency thermoacoustic emissions and generate ultrasound images.

Robustness of range estimates to microscopic heterogeneities should improve as wavelength increases, although accuracy of range estimates computed via one-way beamforming will decrease. To overcome the classic diffraction limit associated with inverse source problems, leveraging *a priori* information may be required. One approach is to use Monte Carlo dose maps computed by the treatment planning system (TPS) to simulate noise-free thermoacoustic emissions simulated for each planning beamlet and then compare to noisy measured emissions [13].

REFERENCES

[1] L. Sulak *et al.*, "Experimental Studies of the Acoustic Signature of Proton Beams Traversing Fluid Media," *Nucl. Instr. Meth.*, vol. 161, pp. 203–217, 1979.

ISBN: 978-3-95450-223-3 ISSN: 2673-7000 doi:10.18429/JACoW-NAPAC2019-TUXBA3

[2] G. A. Askariyan, B. A. Dolgoshein, A. N. Kalinovsky, and N. V. Mokhov, "Acoustic detection of high energy particle showers in water," *Nucl. Instr. Meth.*, vol. 164, no. 2, pp. 267–278, Aug. 1979.

[3] J. Tada, Y. Hayakawa, K. Hosono, and T. Inada, "Time resolved properties of acoustic pulses generated in water and in soft tissue by pulsed proton beam irradiation-A possibility of doses distribution monitoring in proton radiation therapy," *Med. Phys.*, vol. 18, no. 6, pp. 1100–1104, 1991.

[4] Y. Hayakawa *et al.*, "Acoustic Pulse Generated in a Patient During Treatment by Pulsed Proton Radiation Beam," *Radiation Oncology Investigations*, vol. 3, pp. 42–45, 1995.

[5] S. Lehrack *et al.*, "Submillimeter ionoacoustic range determination for protons in water at a clinical synchrocyclotron," *Physics in Medicine & Biology*, vol. 62, no. 17, p. L20, 2017.

[6] P. N. Ostroumov *et al.*, "Compact Carbon Ion Linac", in *Proc. North American Particle Accelerator Conf. (NA-PAC'16)*, Chicago, IL, USA, Oct. 2016, pp. 61-63.

[7] K. Parodi, "Tracking proton therapy with acoustic waves," *Phys. World,* `https://physicsworld.com/a/tracking-proton-therapy-with-acoustic-waves/`.

[8] S. Hickling *et al.*, "Ionizing radiation-induced acoustics for radiotherapy and diagnostic radiology applications," *Med. Phys.*, vol. 45, no. 7, pp. e707–e721, Apr. 2018.

[9] S. Kellnberger *et al.*, "Ionoacoustic tomography of the proton Bragg peak in combination with ultrasound and optoacoustic imaging," *Scientific Reports*, vol. 6, p. 29305, 2016.

[10] S. Patch *et al.*, "Thermoacoustic Range Verification using a Clinical Ultrasound Array Provides Perfectly co-Registered Overlay of the Bragg peak onto an Ultrasound Image," *Physics in Medicine and Biology*, vol. 61, pp. 5621–5638, 2016.

[11] R. C. Pardo, G. Savard, and R. V. F. Janssens, "ATLAS with CARIBU: A Laboratory Portrait," *Nucl. Phys. News*, vol. 26, no. 1, pp. 5–11, Jan. 2016.

[12] S. K. Patch, D. Santiago-Gonzalez, and B. Mustapha, "Thermoacoustic range verification in the presence of acoustic heterogeneity and soundspeed errors - Robustness relative to ultrasound image of underlying anatomy.," *Med. Phys.*, vol. 46, pp 318-327, 2018.

[13] S. K. Patch, D. E. M. Hoff, T. B. Webb, L. G. Sobotka, and T. Zhao, "Two-stage ionoacoustic range verification leveraging Monte Carlo and acoustic simulations to stably account for tissue inhomogeneity and accelerator-specific time structure - A simulation study.," *Med Phys*, vol. 45, no. 2, pp. 783–793, Feb. 2018.

[14] F. Duck, *Physical Properties of Tissue*. London, San Diego: Academic Press, 1990.

[15] F. John, *Partial Differential Equations*, 4th ed., New York, NY: Springer, 1981, pp. 135–136.

[16] F. Alsanea, V. Moskvin, and K. M. Stantz, "Feasibility of RACT for 3D dose measurement and range verification in a water phantom," *Med Phys*, vol. 42, no. 2, pp. 937–46, Feb. 2015.

[17] K. C. Jones, C. M. Seghal, and S. Avery, "How proton pulse characteristics influence protoacoustic determination of proton-beam range: simulation studies," *Physics in Medicine and Biology*, vol. 61, no. 6, p. 2213, 2016.

Content from this work may be used under the terms of the CC BY 3.0 licence (© 2019). Any distribution of this work must maintain attribution to the author(s), title of the work, publisher, and DOI